

Thermoelectric properties of Ba-Cu-Si clathrates

X. Yan,^{1,2} M. X. Chen,^{3,4} S. Laumann,¹ E. Bauer,¹ P. Rogl,² R. Podloucky,³ and S. Paschen^{1,*}

¹*Institute of Solid State Physics, Vienna University of Technology, Wiedner Hauptstr. 8-10, 1040 Vienna, Austria.*

²*Institute of Physical Chemistry, University of Vienna, Währingerstr. 42, 1090 Vienna, Austria.*

³*Institute of Physical Chemistry, University of Vienna, Sensengasse 8/7, 1090 Vienna, Austria.*

⁴*Center for Computational Materials Science, University of Vienna, Sensengasse 8/7, 1090 Vienna, Austria*

(Dated: July 17, 2018)

Thermoelectric properties of the type-I clathrates $\text{Ba}_8\text{Cu}_x\text{Si}_{46-x}$ ($3.6 \leq x \leq 7$, $x =$ nominal Cu content) are investigated both experimentally and theoretically. The polycrystalline samples are prepared either by melting, ball milling and hot pressing or by melt spinning, hand milling and hot pressing techniques. Temperature-dependent electrical resistivity, $\rho(T)$, and the Seebeck coefficient, $S(T)$, measurements reveal metal-like behavior for all samples. For $x = 5$ and 6, density functional theory calculations are performed for deriving the enthalpy of formation and the electronic structure which is exploited for the calculation of Seebeck coefficients and conductivity within Boltzmann's transport theory. For simulating the properties of doped clathrates the rigid band model is applied. On the basis of the density functional theory results the experimentally observed compositional dependence of $\rho(T)$ and $S(T)$ of the whole sample series is analyzed. The highest dimensionless thermoelectric figure of merit ZT of 0.28 is reached for a melt-spun sample at 600°C . The relatively low ZT values in this system are attributed to the too high charge carrier concentrations.

I. INTRODUCTION

Intermetallic clathrates have been investigated extensively in recent years as promising thermoelectric materials¹. They crystallize in several structure types², of which the type I clathrates A_8E_{46} (A = alkali, alkaline earth, or rare earth element, E = group IV element) have hitherto shown the best thermoelectric performance. The unique features of the clathrate crystal structure are generally regarded as ideal realization of the phonon glass – electron crystal (PGEC) concept¹. Clathrates are viewed as Zintl compounds^{3,4}: the covalently bonded framework atoms (E) use the valence electrons of the guest atoms (A) to satisfy the octet rule and to acquire closed-shell electronic configurations. Simple electron counting based on the Zintl concept⁵ frequently works well^{3,4,6,7} for understanding the thermoelectric properties of clathrates. Previously, most investigations focused on clathrates with heavy framework atoms (e.g., Ge- or Sn-based clathrates) which typically are partially substituted by other heavy elements (e.g., Ga, In, or transition metal elements). Comparably little work has been done on Si-based clathrates^{8–15}, despite the technological interest in this low-cost element. Early interest in Si-based clathrates was triggered by the discovery of superconductivity in $\text{Na}_2\text{Ba}_6\text{Si}_{46}$ with a critical temperature $T_c = 4$ K (Ref. 16). Later on, investigations on $\text{Ba}_8\text{TM}_x\text{Si}_{46-x}$ (TM: transition metal element, TM = Cu, Ag, Au)^{17–21} demonstrated the stabilization of the crystal structure by TM substitution, allowing for a simple synthesis in an arc furnace. However, this led to a suppression of T_c which, from band structure calculations, could be attributed to a change of the density of states near the Fermi level^{22–24}. Interest in the thermoelectric properties of TM-containing clathrates also arose from band structure calculations which indicated that $\text{Ba}_8\{\text{Cu,Ag,Au}\}_6\text{Si}_{40}$ clathrates are degenerate p -

type semiconductors with large Seebeck coefficients at room temperature^{23,25,26}. This motivated us to investigate the thermoelectric properties of $\text{Ba}_8\text{Cu}_x\text{Si}_{46-x}$ in detail.

Recently, we investigated the phase equilibrium of clathrates in the Ba–Cu–Si system at 800°C and its crystal structure²⁷. On the other hand, first-principles methods have made considerable successes in studies of structural and electronic properties of materials. Moreover, the Boltzmann transport theory has been extensively applied to investigate electronic transport properties such as electrical conductivity and Seebeck coefficient. A method that hybridize the first-principle methods and Boltzmann theory would no doubt benefit understanding of thermoelectric properties of materials, which has proved to be quite successful in our recent work²⁸. In this paper, we present a comprehensive study on the thermoelectric properties of $\text{Ba}_8\text{Cu}_x\text{Si}_{46-x}$ ($3.6 \leq x \leq 7$, $x =$ nominal Cu content) in combination with density functional theory (DFT) calculations and the semi-classic Boltzmann transport equations.

II. EXPERIMENTAL

A. Sample preparation and characterization

A series of clathrates, with the nominal compositions $\text{Ba}_8\text{Cu}_x\text{Si}_{46-x}$ ($x = 3.6, 3.8, 4.2, 4.4, 4.6, 5, 6, 7$, denoted by HP01-HP08), was prepared in a high-frequency induction furnace from high-purity elements (more than 99.9 mass%), as described previously²⁷. The samples were subsequently annealed (800°C , 15 days), ball milled and hot pressed ($T = 800^\circ\text{C}$, $P = 56$ MPa, time = 2 hours). A sample with $x = 6$ was chosen for melt spinning^{29,30} with wheel speeds of 1500 r/min and 2500 r/min (samples MS1500 and MS2500).

X-ray powder diffraction (XPD) data for all samples were collected using a Siemens D5000 diffractometer (Cu $K_{\alpha 1,2}$, $10^\circ \leq 2\theta \leq 110^\circ$) and processed with the Rietveld method using the program FULLPROF³¹. The crystallite size of hot pressed samples was evaluated from the X-ray diffraction patterns using the MDI jade 5.0 software (Materials Data Inc., Liverpool, CA). Annealed (300°C, 1 day) pure Si powder was used for the evaluation of the peak broadening due to the X-ray instrument. The bulk density of the hot pressed samples was measured by the Archimedes method.

The compositions of the hot pressed samples were determined by energy dispersive X-ray spectroscopy (EDX) in a scanning electron microscope (SEM) operated at 20 kV (Philips XL30 ESEM; JEOL JSM-T330A, probe size: 1 μm).

B. Physical properties

The electrical resistivity and the Seebeck coefficient were measured with a ZEM-3 (ULVAC-Riko, Japan). The thermal conductivity was calculated from the thermal diffusivity D_t , measured by a laser flash method with a Flashline-3000 (ANTER, USA), the specific heat C_p and the bulk density D using the relation $\kappa = D_t C_p D$. Hall effect measurements were performed with a standard ac technique in a physical property measurement system (PPMS, Quantum Design) in the temperature range from 2 to 300 K in magnetic fields up to 9 T.

C. Computational details

Density functional theory (DFT) calculations were carried out by the Vienna *ab initio* Simulation Package (VASP)^{32,33}. The exchange-correlation functional is approximated within the generalised gradient approximation using the parametrization of Perdew, Burke, and Ernzerhof (PBE). The electron-ion interaction is treated within the framework of Blöchl's projector augmented wave method^{34,35}. The valence state configurations for the construction of the pseudopotentials included $5s^2 5p^6 6s^2$ states for Ba, $3p^6 3d^{10} 3s^1$ states for Cu, and $3s^2 3p^2$ states for Si. For all calculations a $5 \times 5 \times 5$ \mathbf{k} point grid according to Monkhorst and Pack³⁶ was used to sample the Brillouin zone.

Transport properties for the electrons were modeled within the semi-classical Boltzmann transport theory in which the Seebeck coefficient tensor (S) and electrical resistivity (ρ) are defined as

$$\rho = \sigma^{-1} \quad \sigma(T, E_F) = e^2 K_0 \quad (1)$$

$$S(T, E_F) = \frac{K_1}{eTK_0} \quad (2)$$

Here K_n is related to electronic structures by

$$K_n = \frac{1}{4\pi^3} \frac{\tau}{\hbar} \sum_{i,\mathbf{k}} \mathbf{v}(i, \mathbf{k}) \mathbf{v}(i, \mathbf{k}) (E(i, \mathbf{k}) - E_F)^n \left(-\frac{\partial f_{E_F}(T, E(i, \mathbf{k}))}{\partial E} \right). \quad (3)$$

The vectors $\mathbf{v} = \partial E(i, \mathbf{k}) / \partial \mathbf{k}$ represent the velocities of the electrons as defined by the derivative of the band energy. τ , f and E_F are the relaxation time, the Fermi function, and the Fermi energy, respectively. Within Boltzmann's transport theory effects of electron-electron and electron-phonon scattering are merged into the relaxation time τ . Because a first-principles calculation of τ is not feasible for systems with large numbers of atoms per unit cell, τ was considered as an empirical parameter by fitting to one selected experimental value at a given temperature, as described below.

It should be noted that the cubic symmetry of $\text{Ba}_8\text{Si}_{40}$ is maintained for $\text{Ba}_8\text{Cu}_6\text{Si}_{40}$ but broken when modeling $\text{Ba}_8\text{Cu}_5\text{Si}_{41}$. Therefore, the Seebeck tensor has now unequal components. Because the experimental samples were produced at higher temperatures the measured structures are always cubic with some random site occupations. In order to enable the comparison with experiment the symmetry average of the calculated Seebeck and conductivity tensor is made, resulting in only one component for each physical property. Concerning the transport properties of $\text{Ba}_8\text{Cu}_5\text{Si}_{41}$ two sets of calculations have been made, namely for a geometrically fully relaxed structure and for a structure denoted as frozen- $\text{Ba}_8\text{Cu}_5\text{Si}_{41}$, for which the high-symmetry structure of $\text{Ba}_8\text{Cu}_6\text{Si}_{40}$ was chosen and no relaxation was allowed. The actual calculations of the transport properties were made by an adapted version of the package BoltzTrap³⁷. For this purpose the Kohn-Sham energy eigenvalues were generated on a very dense $25 \times 25 \times 25$ \mathbf{k} -point grid.

III. RESULTS AND DISCUSSION

A. Sample purity in the hot pressed samples and structural details of clathrates

The phase constitutions of all hot pressed samples agree well with the isothermal section of the system Ba-Cu-Si at 800°C (the homogeneity range of the clathrate at 800°C: $3.4(1) \leq x_{\text{Cu}} \leq 4.8(1)$, Ref. 27), except for a very small amount of Si (and/or of holes) that is uniformly dispersed in the main clathrate phase (even for the samples with $x \geq 5$). The compositions from EDX measurements are close to the nominal compositions for the samples HP01-HP05 which correspond to the single phase range of clathrate in the phase diagram. For the samples HP06-HP08, a composition of $\text{Ba}_{8.1}\text{Cu}_{4.9}\text{Si}_{41.0}$ is determined. Table I summarizes the nominal Cu content, the Cu contents determined from EDX and from the XRD refinements, as well as the crystallite sizes and densities of all specimens.

TABLE I. Hot pressed $\text{Ba}_8\text{Cu}_x\text{Si}_{46-x}$ samples with their nominal Cu content (x_{nom}), the Cu content determined from EDX measurements (x_{EDX}) and from the XRD refinements (x_{ref}), the bulk density (D_b) and the crystallite size (S_c).

Name	x_{nom}	x_{EDX}	x_{ref}	D_b (%)	S_c (nm)
HP01	3.6	3.5	3.61	92.7	165(15)
HP02	3.8	3.7	3.85	92.8	125(10)
HP03	4.2	4.2	4.29	92.0	120(5)
HP04	4.4	4.3	4.38	88.7	130(10)
HP05	4.6	4.5	4.55	91.8	135(15)
HP06	5.0	4.9	4.72	95.0	140(15)
HP07	6.0	4.9	4.88	96.6	155(5)
HP08	7.0	4.9	4.98	92.5	160(10)
MS1500	6.0	4.8	4.84	90.4	
MS2500	6.0	4.8	4.82	88.1	

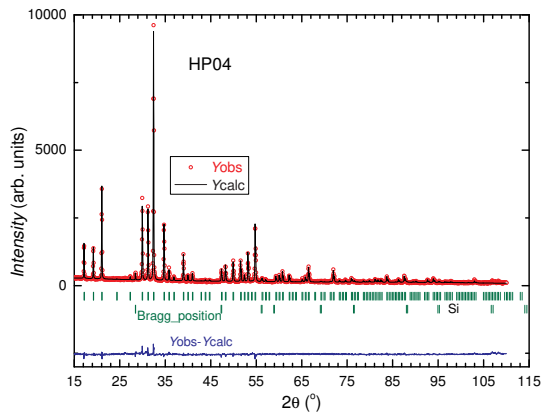


FIG. 1. (Color online) The Rietveld refinement of the powder X-ray diffraction data from HP04 shows the main clathrate phase with a small amount of Si. The microstructure of this sample (insert) shows the main grey phase (clathrate phase) with black spots (Si and/or holes).

Rietveld refinements of the X-ray diffraction data were performed with an initial model derived from the single crystal X-ray diffraction data of $\text{Ba}_8\text{Cu}_5\text{Si}_{41}$ (Ref. 27). Here, Ba atoms fully occupy the $2a$ and $6c$ sites in the crystal structure of the type-I clathrate, Cu atoms share the $6d$ site with Si, and the remaining sites are occupied by Si atoms. For this model the Rietveld refinements of the data for all samples have high reliabilities and yield reasonable structure parameters (see Table II). Unlike for the case of several Ge-based TM clathrates^{8,38–45}, here no vacancy could be identified at the $6d$ site within experimental resolution. Figure 1 shows the Rietveld refinement for the sample HP04 as an example.

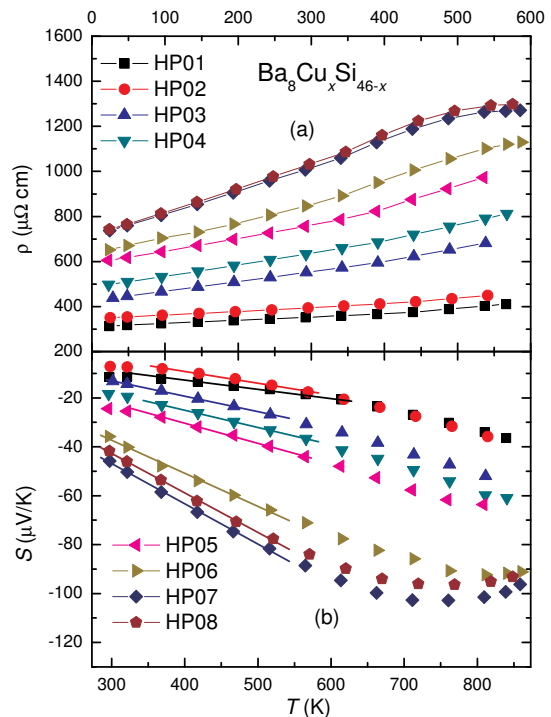


FIG. 2. (Color online) Temperature dependent electrical resistivity, $\rho(T)$, and Seebeck coefficient, $S(T)$, for $\text{Ba}_8\text{Cu}_x\text{Si}_{46-x}$ ($3.6 \leq x \leq 7$) plotted as a function of temperature. The straight lines in $S(T)$ represent linear fits through the origin.

B. Thermoelectric properties

1. Hot pressed $\text{Ba}_8\text{Cu}_x\text{Si}_{46-x}$ samples

The temperature dependent electrical resistivity, $\rho(T)$, and Seebeck coefficient, $S(T)$, of the hot pressed samples show a systematic evolution with the Cu content (Fig. 2). All samples show metal-like behavior. The negative $S(T)$ values indicate that electrons dominate the transport properties. In the Cu-rich samples (HP06–HP08), extrema are observed in $\rho(T)$ and $S(T)$.

The overall variation of $\rho(T)$ and $S(T)$ with Cu content can be qualitatively understood within a phenomenological picture of the electronic band structure of TM containing clathrates²³. In all samples, the Fermi level lies within the conduction band. This explains the metal-like behavior of $\rho(T)$ and the negative $S(T)$ values. With increasing x , the Fermi level moves towards the edge of the conduction band. Thereby, the charge carrier concentration n decreases and, consequently, the absolute values of $\rho(T)$ and $S(T)$ increase.

According to band structure calculations for a fully ordered structure, $\text{Ba}_8\text{Cu}_6\text{Si}_{40}$ should be a p -type semiconductor (see Sect. III C and Refs. 25 and 26). The fact that only n -type behavior is found in our sample series is attributed to the formation of competing phases when x_{nom} exceeds 4.9. This inhibits a further energetical low-

TABLE II. Structure data for $\text{Ba}_8\text{Cu}_x\text{Si}_{46-x}$ ($3.6 \leq x \leq 7$). The data have been standardized by the program Structure Tidy⁴⁶.

Name	HP01	HP02	HP03	HP04
x_{ref}	3.61	3.85	4.29	4.38
a (nm), Guinier	1.03272(3)	1.03273(5)	1.03278(3)	1.03277(6)
$R_F = \sum F_o - F_c / \sum F_o$	0.105	0.122	0.082	0.075
$R_I = \sum I_o - I_c / \sum I_o$	0.085	0.081	0.073	0.060
Ba1, in $2a$ (0, 0, 0) B_{eq} (B_{iso}) $10^2(\text{nm}^2)$	0.41(9)	0.62(9)	0.47(9)	0.41(7)
Ba2, in $6c$ ($\frac{1}{4}, 0, \frac{1}{2}$) B_{eq} (B_{iso}) $10^2(\text{nm}^2)$	1.71(9)	1.72(9)	1.63(8)	1.57(5)
M1, in $6d$ ($\frac{1}{4}, \frac{1}{2}, 0$), Occ.	3.61(7)Cu+2.39Si	3.85(6)Cu+2.15Si	4.29(6)Cu+1.71Si	4.38(5)Cu+1.62Si
B_{eq} (B_{iso}) $10^2(\text{nm}^2)$	0.32(8)	0.43(9)	0.42(9)	0.53(9)
Si1 in $16i$ (x, x, x), x	0.1855(3)	0.1854(3)	0.1852(3)	0.1851(2)
B_{eq} (B_{iso}) $10^2(\text{nm}^2)$	0.54(7)	0.85(9)	0.59(9)	0.66(9)
Si2 in $24k$ (0, y, z), y, z	0.1198(5), 0.3077(5)	0.1188(4), 0.3091(5)	0.1189(4), 0.3098(5)	0.1192(3), 0.3094(3)
B_{eq} (B_{iso}) $10^2(\text{nm}^2)$	0.43(9)	0.25(7)	0.43(9)	0.27(9)

TABLE III. continued

Name	HP05	HP06	HP07	HP08
x_{ref}	4.55	4.72	4.88	4.98
a (nm), Guinier	1.03280(3)	1.03286(4)	1.03285(5)	1.03287(4)
$R_F = \sum F_o - F_c / \sum F_o$	0.107	0.088	0.083	0.088
$R_I = \sum I_o - I_c / \sum I_o$	0.086	0.071	0.071	0.065
Ba1, in $2a$ (0, 0, 0) B_{eq} (B_{iso}) $10^2(\text{nm}^2)$	0.49(7)	0.41(9)	0.38(9)	0.40(9)
Ba2, in $6c$ ($\frac{1}{4}, 0, \frac{1}{2}$) B_{eq} (B_{iso}) $10^2(\text{nm}^2)$	1.63(6)	1.55(9)	1.52(7)	1.63(8)
M1, in $6d$ ($\frac{1}{4}, \frac{1}{2}, 0$), Occ.	4.55(5)Cu+1.45Si	4.72(7)Cu+1.28Si	4.88(6)Cu+1.12Si	4.98(5)Cu+1.02Si
B_{eq} (B_{iso}) $10^2(\text{nm}^2)$	0.65(9)	0.68(8)	0.43(9)	0.86(9)
Si1 in $16i$ (x, x, x), x	0.1842(2)	0.1849(3)	0.1848(3)	0.1849(3)
B_{eq} (B_{iso}) $10^2(\text{nm}^2)$	0.68(9)	0.62(9)	0.65(9)	0.68(9)
Si2 in $24k$ (0, y, z), y, z	0.1203(3), 0.3096(2)	0.1190(5), 0.3093(5)	0.1200(4), 0.3095(4)	0.1195(3), 0.3092(3)
B_{eq} (B_{iso}) $10^2(\text{nm}^2)$	0.40(9)	0.52(9)	0.28(7)	0.39(9)

ering of the Fermi level down to the valence band. The energy gap is predicted to decrease with increasing Cu content (see Sect. III C and Refs. 25 and 26). This is in agreement with the observed maxima in $\rho(T)$ and $S(T)$ for the Cu-rich samples HP06-08, which signal the onset of intrinsic conduction above about 500°C.

To a first approximation, for temperatures above the Debye temperature θ_D ($\theta_D \approx 150^\circ\text{C}$ for $\text{Ba}_8\text{Cu}_5\text{Si}_{41}$, Ref. 47), and ignoring the phonon-drag contribution to the total Seebeck coefficient⁴⁸, $S(T)$ should vary linearly with temperature as⁴⁹

$$S = \frac{2\pi^2 k_B^2 m_e}{e\hbar^2 (3n\pi^2)^{2/3}} T \quad (4)$$

where n is the charge carrier concentration, m_e is the free-electron mass, e is its charge and the other symbols have their usual meaning. Thus, one should be able to estimate n from the slopes of linear fits to $S(T)$. These fits are shown as straight lines in Fig. 2. For high Cu contents, these fits describe the data quite well in relatively broad temperature ranges. For low Cu contents,

the agreement is poorer. As will be shown below, this can be attributed to a temperature dependent charge carrier concentration.

For the samples HP01, HP02, HP04 and HP06 we have also determined the charge carrier concentrations more directly, by measurements of the Hall coefficient $R_H(T)$ below 300 K. The charge carrier concentrations calculated using a simple one-band model $n_H = 1/(eR_H)$, are plotted against temperature in Fig. 3. For HP06, $n_H(T)$ is almost temperature independent. For the Cu-poor samples, on the other hand, $n_H(T)$ shows a sizable temperature dependence.

Finally, we can derive the charge carrier concentration expected within a simple Zintl electron counting scheme. For $\text{Ba}_8\text{Cu}_x\text{Si}_{41-x}$, the charge carrier concentration per unit cell, n_Z , varies with x as $n_Z(x) = 16 - 3x$, if the oxidation states +2, -3, and 0 are assumed for Ba, Cu and Si²⁴, respectively. A comparison of the charge carrier concentration determined via all above methods is shown in Fig. 4.

The temperature dependent thermal conductivity,

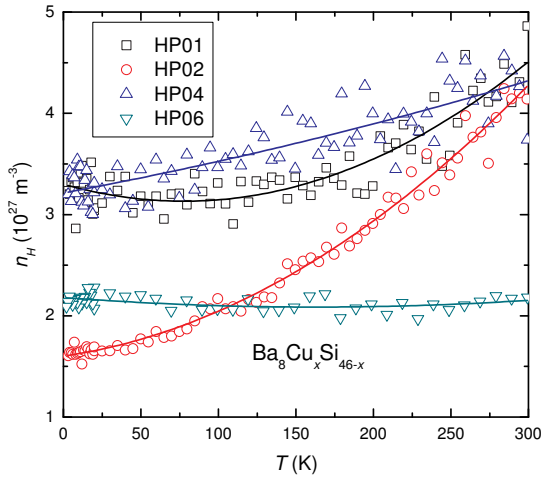


FIG. 3. (Color online) Temperature dependent charge carrier concentration $n_H(T)$ of HP01, HP02, HP04 and HP06 derived from Hall effect measurements in a one-band model. The lines are guides to the eye.

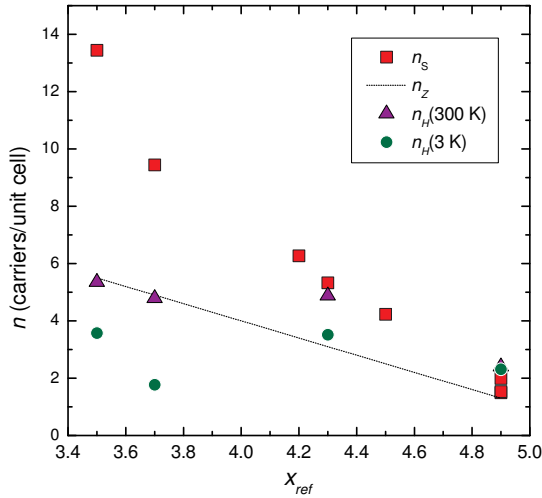


FIG. 4. (Color online) Charge carrier concentrations derived from different methods (see text) vs x_{EDX} .

$\kappa(T)$, varies systematically with x , as shown in Fig. 5(a). In Fig. 5(b) and (c), we plot the temperature dependent electronic component $\kappa_e(T)$ and the lattice component $\kappa_L(T)$, respectively. κ_e is estimated via the Wiedemann-Franz law $\kappa_e = L_0 T / \rho$, where $L_0 = 2.44 \times 10^{-8} \text{ (V/K)}^2$, from the electrical resistivity ρ . κ_L is the difference between κ and κ_e . The dominating contribution to κ changes from κ_e to κ_L with increasing Cu content, with almost half to half contributions for the samples HP05 to HP08. For $\kappa_L(T)$ three different characteristics can be distinguished beyond the experimental uncertainties, as indicated by the gray shadows shown in Fig. 5(c).

The Cu-poor samples have the strongest temperature dependence and the lowest κ_L values. With increasing x_{EDX} and thus decreasing charge carrier concentration (at elevated temperatures), this dependence be-

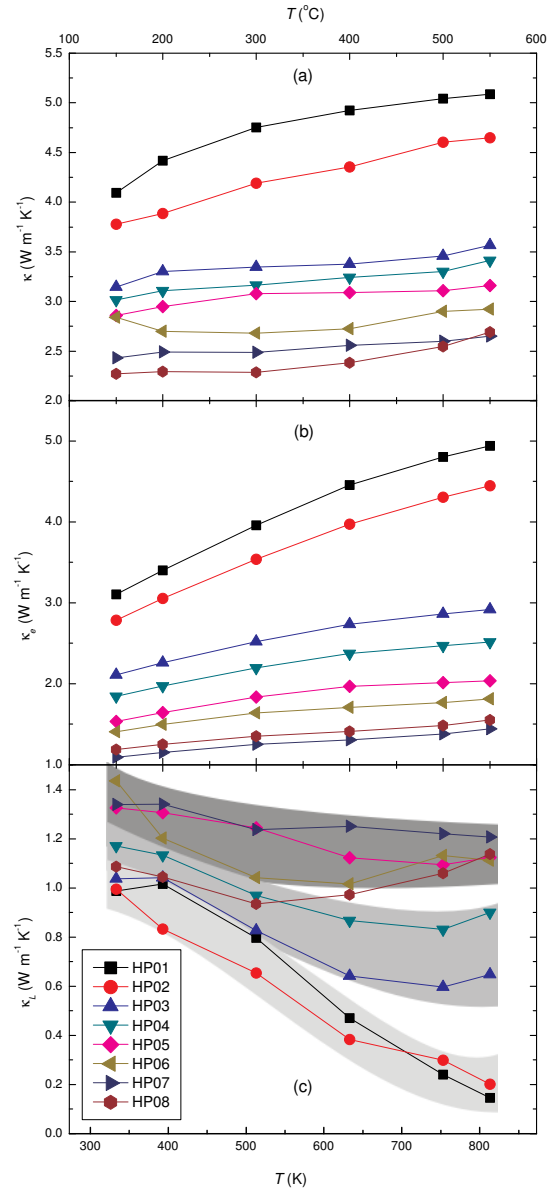


FIG. 5. (Color online) Temperature dependent total thermal conductivity $\kappa(T)$ in (a), electronic contribution $\kappa_e(T)$ in (b) and lattice contribution $\kappa_L(T)$ in (c) for $\text{Ba}_8\text{Cu}_x\text{Si}_{46-x}$ ($3.6 \leq x \leq 7$). The gray shadows in (c) indicated different characteristics in $\kappa_L(T)$ (see text).

comes more gradual and κ_L rises. This trend cannot result from point scattering or boundary scattering since the crystallite size and bulk density do not vary systematically with x_{EDX} (Table I). Instead suggest that, besides phonon-phonon scattering that usually is the dominating scattering at high temperature⁵⁰, here also electron-phonon scattering contributes sizably. An alternative explanation for the experimentally observed trend could be that the presence of more atoms Cu disturbs the resonant scattering of the guest atoms in the large cage.

The dimensionless thermoelectric figure of merit $ZT = S^2 T / \rho \kappa$ is plotted against temperature in Fig. 6(a). ZT

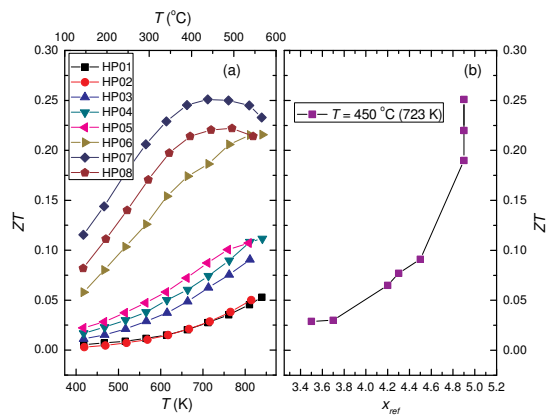


FIG. 6. (Color online) (a) Figure of merit ZT for $\text{Ba}_8\text{Cu}_x\text{Si}_{46-x}$ ($3.6 \leq x \leq 7$) versus temperature T . (b) ZT vs. x_{EDX} at $T = 450^\circ\text{C}$.

depends sensitively on x_{EDX} , especially for the Cu-rich side (Fig. 6). Surprisingly, the samples HP06–HP08 with highest x_{EDX} and a small amount of foreign phases show the highest ZT values in the investigated temperature range. The highest ZT of 0.25 is reached for sample HP07 at about 450°C . Between 350 to 550°C , ZT remains above 0.23.

2. Melt-spun $\text{Ba}_8\text{Cu}_6\text{Si}_{40}$

In order to further optimize ZT of the clathrates in the Ba–Cu–Si system, we melt-spun an as cast sample of $\text{Ba}_8\text{Cu}_6\text{Si}_{40}$ with two different Cu wheel speeds, 1500 and 2500 r/min. The resulting ribbons were hand milled rather than ball milled to retain the microstructure of the ribbons to the largest possible extent, and then hot pressed. These samples are denoted by MS1500 and MS2500. Figure 7 shows $\rho(T)$, $S(T)$, $\kappa(T)$ and $ZT(T)$ of MS1500 and MS2500, together with the corresponding data for the conventionally prepared sample HP07 of the same nominal composition. While the sample HP07 reaches the largest absolute S values in the measured temperature range, $|S(T)|$ of the melt-spun samples is still increasing the temperature. The sample MS2500 has the lowest ρ in the measured temperature but also here a maximum in $\rho(T)$ appears to be reached at lower temperatures for HP07 than for the melt-spun samples. MS1500 shows the lowest $\kappa(T)$. Above 480°C , MS1500 has the highest ZT value.

As seen from Fig. 7(b), $S(T)$ is very similar for MS1500 and MS2500. This indicates that also the charge carrier concentrations are comparable: the values $1.88 \times 10^{27} \text{ m}^{-3}$ for MS2500 and $1.86 \times 10^{27} \text{ m}^{-3}$ for MS1500 are derived from linear fits to $S(T)$ using Eqn. 4 as done above. Hall effect measurements also yield similar n_H within the above used one-band model: $2.18 \times 10^{27} \text{ m}^{-3}$ for MS2500 and $2.11 \times 10^{27} \text{ m}^{-3}$ for MS1500. The more pronounced differences between MS2500 and MS1500 in

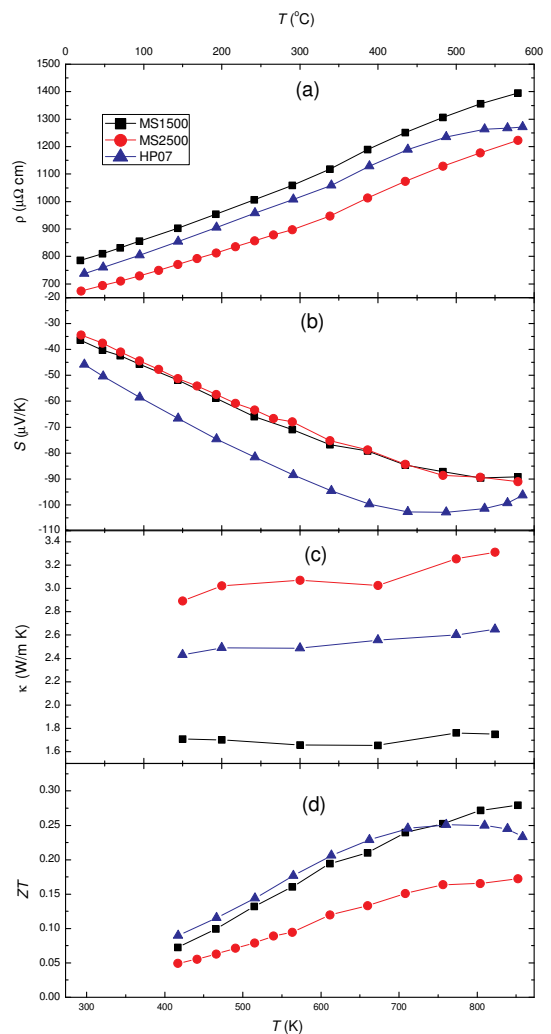


FIG. 7. (Color online) Temperature dependent electrical resistivity, $\rho(T)$, in (a), Seebeck coefficient, $S(T)$, in (b), thermal conductivity, $\kappa(T)$, in (c) and figure of merit, $ZT(T)$, in (d) of $\text{Ba}_8\text{Cu}_6\text{Si}_{40}$ prepared via different preparation routes (see text).

$\rho(T)$ and κ must therefore be attributed to the different charge carrier mobilities $\mu_H(T) = R_H(T)/\rho(T)$, which are 2.4 and $3.5 \text{ cm}^2/\text{Vs}$ at 300 K for MS1500 and MS2500, respectively. We attribute that to a smaller average grain size in MS1500 than in MS2500.

C. DFT results

1. Structure and energetics

The lattice parameters for the cubic type I clathrate structure are derived from fully relaxed VASP calculations, from which also the enthalpies of formation ΔH in terms of differences of total energies at zero pressure are derived. We compare our calculations on $\text{Ba}_8\text{Cu}_x\text{Si}_{46-x}$ with a recent study on the type I clathrate

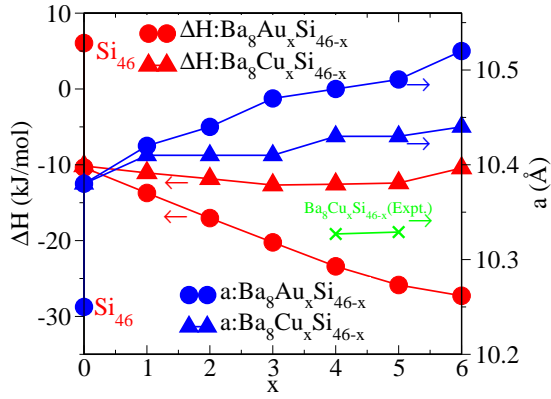


FIG. 8. DFT derived formation energies ΔH and lattice parameters of $\text{Ba}_8\text{Au}_x\text{Si}_{46-x}$ (balls) and $\text{Ba}_8\text{Cu}_x\text{Si}_{46-x}$ (triangles) as a function of doping. Also shown are the results for the unfilled cage structure of Si_{46} .

$\text{Ba}_8\text{Au}_x\text{Si}_{46-x}$. Figure 8 shows formation enthalpies and lattice parameters for four types of systems, namely Si_{46} , $\text{Ba}_8\text{Si}_{46}$, $\text{Ba}_8\text{Cu}_x\text{Si}_{46-x}$ and $\text{Ba}_8\text{Au}_x\text{Si}_{46-x}$ with $x = 1$ to 6. From the measured X-ray data it was concluded that the Cu atoms are randomly distributed on Si 6d sites due to the preparation at elevated temperatures. However, for the DFT calculations the doping atoms have to be placed on specific sites within the unit cell which, in general, causes changes of lattice symmetry and cell shape. Therefore, to be consistent with experiment a cubic unit cell was enforced for all calculations. More details are given in Refs 28. Comparing to the two experimental data points for the lattice parameter in Fig. 8, one finds that the DFT derived values are larger by about 1%, but show the same trend of increasing with increasing x . The (rather small) difference between first principles theory and experiment is attributed to the approximation for the exchange correlation functional. For the Au-doped compounds the enthalpy of formation decreases (i.e. bonding is enhanced) with increasing Au content, which is very similar to the results for $\text{Ba}_8\text{Ag}_x\text{Ge}_{46-x}$ ²⁸. The trend for the Cu-doped compounds is quite different, because ΔH remains rather constant with increasing x . A more careful examination reveals that ΔH slightly increases for $x > 5$ implying that a doping level x exceeding 5 is unfavorable. This is consistent with the experimental fact that no compound can be stabilized for such large dopings.

2. Electronic properties

The electronic densities of states for $\text{Ba}_8\text{Cu}_x\text{Si}_{46-x}$ are shown in Fig. 9. Significant changes induced by doping Cu are observed. On filling Ba into the voids of the Si_{46} cage the gap is maintained but shrinks in size due to hybridization between Ba and Si states. The gap decreases significantly by adding Cu, which implies hybridization

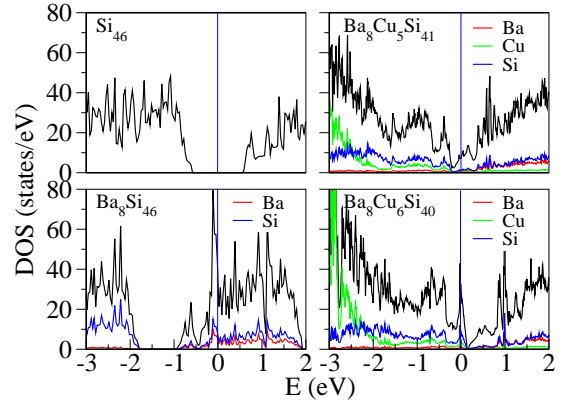


FIG. 9. Density of states (DOS) of $\text{Ba}_8\text{Cu}_x\text{Si}_{46-x}$ ($x = 0, 5$ and 6). Fermi energy at $E = 0$ eV.

between dopants and the Si framework. For $\text{Ba}_8\text{Cu}_5\text{Si}_{41}$ there are two peaks in the DOS around the Fermi energy, which is located at a satellite of the higher energy peak. Doping of Cu up to 6 atoms lowers the higher energy peak in $\text{Ba}_8\text{Cu}_6\text{Si}_{40}$ in magnitude and moves the Fermi energy to the center of the peak at lower energy. The small difference in the shape of the DOS peaks between these two compounds may be due to their different crystal symmetries. However, there is also a significant similarity between $\text{Ba}_8\text{Cu}_5\text{Si}_{41}$ and $\text{Ba}_8\text{Cu}_6\text{Si}_{40}$ in that the peaks around the Fermi energy remain almost unchanged and also the pseudogap occurs for both of them. The similarity of the DOS features justifies the rigid band approximation when varying the atomic composition in terms of changing the number of valence electrons by shifting the Fermi energy. For the validity of the rigid band model the change of the number of valence electrons must be sufficiently small.

The location of the Fermi level plays an important role in understanding transport properties as discussed later. In our recent work within the rigid band approximation²⁸, based on the semiconducting parent compounds of Ge_{46} a simple electron counting rule was proposed: $x_{gap} = \frac{16}{4-n}$ (n is the valency of the dopant) is replaced the Fermi energy in the gap for $\text{Ba}_8\text{M}_x\text{Ge}_{46-x}$. This counting rule can also be applied to $\text{Ba}_8\text{M}_x\text{Si}_{46-x}$ because of the similarity of Si and Ge. For $\text{M} = \text{Cu}$ (i.e. the valency n equals 1) $x_{gap} = 16/3$ is derived, which corresponds very well to experimental concentrations at which the Seebeck coefficient undergoes a drastic change in size.

3. Transport properties

For small variations of the dopant concentration (i.e. variation Δn of the number of valence electrons) the rigid

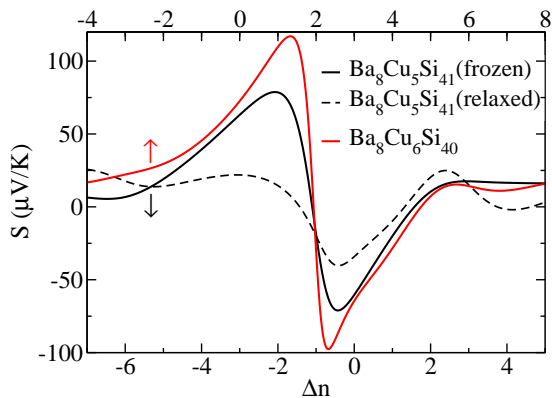


FIG. 10. Calculated Seebeck coefficient at 300 K for $\text{Ba}_8\text{Cu}_5\text{Si}_{41}$ and $\text{Ba}_8\text{Cu}_6\text{Si}_{40}$ as a function of doping Δn . A negative value corresponds to hole doping.

band approximation was employed according to

$$N = \int_{-\infty}^{\infty} g(E)f(T, \mu)dE \quad (5)$$

for calculating the chemical potential μ (i.e. the Fermi energy) for $N = N_0 + \Delta n$ electrons. The number N_0 represents the number of valence electrons of the chosen reference compound with its DOS, $g(E)$. In the Ba–Cu–Si clathrates, Ba, Cu and Si contribute 2, 1 and 4 valence electrons to the system, respectively. For comparing the calculations with measurements on the most interesting experimental sample with composition $\text{Ba}_8\text{Cu}_{4.9}\text{Si}_{41.1}$, $\Delta n = 0.3$ if $\text{Ba}_8\text{Cu}_5\text{Si}_{41}$ is chosen as the reference and $\Delta n = 3.3$ if $\text{Ba}_8\text{Cu}_6\text{Si}_{40}$ is the reference.

Figure 10 depicts the calculated Seebeck coefficients at 300 K vs. chemical doping for relaxed- and frozen- $\text{Ba}_8\text{Cu}_5\text{Si}_{41}$ and $\text{Ba}_8\text{Cu}_6\text{Si}_{40}$, which change sign as the Fermi level crosses the gap. There is a significant difference in the amplitudes of the Seebeck coefficient between the relaxed and frozen structures of $\text{Ba}_8\text{Cu}_5\text{Si}_{41}$ revealing the influence of structural relaxation. The Seebeck coefficient of frozen- $\text{Ba}_8\text{Cu}_5\text{Si}_{41}$ resembles quite well that of $\text{Ba}_8\text{Cu}_6\text{Si}_{40}$, indicating that the rigid band approximation should be useful when varying x between 5 and 6. Both curves agree very well with each other except for the absolute values nearby the gap. However, the Seebeck coefficients are significantly different for the fully relaxed structures. This is different from the comparison of Seebeck coefficients of $\text{Ba}_8\text{Ag}_5\text{Si}_{41}$ and $\text{Ba}_8\text{Ag}_6\text{Si}_{40}$ with their fully relaxed structures, because these practically coincide.²⁸

Figures 11 and 12 depict the calculated temperature-dependent Seebeck coefficients $S(T)$ for $\text{Ba}_8\text{Cu}_x\text{Si}_{46-x}$, which are obviously very sensitive to doping. For comparison, S for $\text{Ba}_8\text{Cu}_{5.4}\text{Si}_{40.6}$ was also calculated by taking $\text{Ba}_8\text{Cu}_6\text{Si}_{40}$ as the reference. Although $S(T)$ for $\text{Ba}_8\text{Cu}_{5.4}\text{Si}_{40.6}$ as derived from the different references are qualitatively similar, there are significant differences

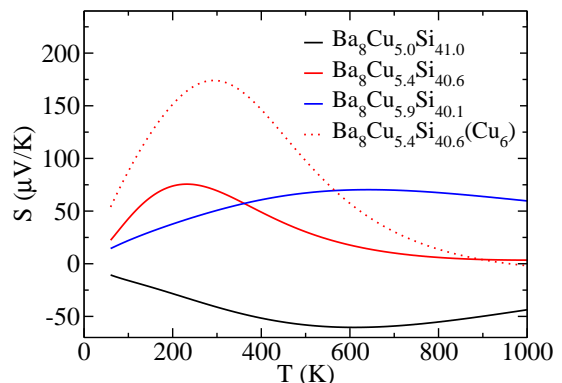


FIG. 11. DFT derived Seebeck coefficients for $\text{Ba}_8\text{Cu}_x\text{Si}_{46-x}$ ($x = 5.0 - 5.9$) as a function of temperature as calculated within the rigid band approximation taking frozen- $\text{Ba}_8\text{Cu}_5\text{Si}_{41}$ as the reference. For $\text{Ba}_8\text{Cu}_{5.4}\text{Si}_{40.6}$ the Seebeck coefficient with $\text{Ba}_8\text{Cu}_6\text{Si}_{40}$ as the reference is also shown for comparison (dotted line).

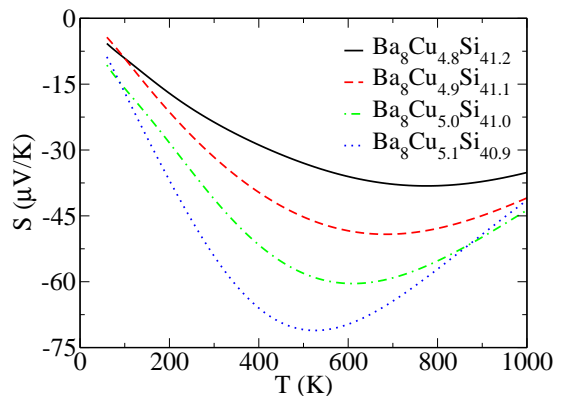


FIG. 12. DFT derived Seebeck coefficients for $\text{Ba}_8\text{Cu}_x\text{Si}_{46-x}$ ($x = 4.8 - 5.1$) as a function of temperature as calculated within the rigid band approximation for which frozen- $\text{Ba}_8\text{Cu}_5\text{Si}_{41}$ is the reference.

concerning the magnitude and the position of the maximum. This suggests that care has to be taken for selecting the reference compound. Apparently, $S(T)$ at low temperatures changes sign when the Cu concentration crosses the critical value of $x_{gap} = 5.33$. The change of sign for $\text{Ba}_8\text{Cu}_x\text{Si}_{46-x}$ can be understood in terms of the Mott's formula, which is a simplification valid at very low temperatures. There, the sign and magnitude of the Seebeck coefficient are determined by the DOS and its derivative with respect to energy at the Fermi energy E_F , $-\frac{dg(E)}{dE} \frac{1}{g(E)}|_{E_F}$, which results in an opposite sign for the Seebeck coefficient and the slope of the DOS at E_F . According to Mott a small $g(E_F)$ together with a large $\frac{dg(E)}{dE}|_{E_F}$ gives rise to a large Seebeck coefficient, and therefore the Fermi energy should be as close as possible to the gap. This consideration is, however, only valid at

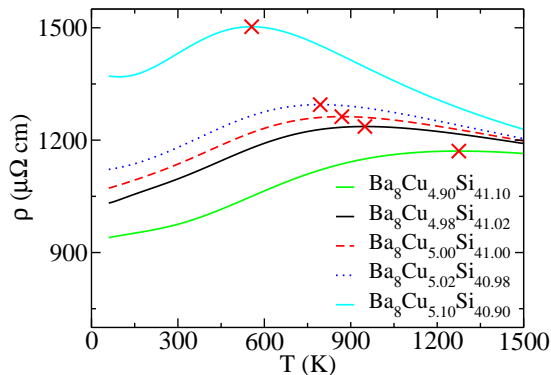


FIG. 13. DFT derived electrical resistivities of $\text{Ba}_8\text{Cu}_x\text{Si}_{46-x}$ within the rigid band approximation with frozen- $\text{Ba}_8\text{Cu}_5\text{Si}_{41}$ as the reference. Crosses denote the positions of the maxima.

sufficiently low temperatures. As temperature increases, the Fermi energy moves towards or away from the gap, thus changing $S(T)$.

From Fig. 9 one derives a positive derivative for $\text{Ba}_8\text{Cu}_5\text{Si}_{41}$ thus producing a negative Seebeck coefficient. For compositions close to $\text{Ba}_8\text{Cu}_5\text{Si}_{41}$, for instance $\text{Ba}_8\text{Cu}_{4.9}\text{Si}_{41.1}$, the valence electron number is 1.3 electron larger than the critical value $x_{gap} = 5.33$, which means that the Fermi energy is above the gap, higher than the Fermi energy of $\text{Ba}_8\text{Cu}_5\text{Si}_{41}$. Further decreasing the Cu concentration, i.e., increasing the number of valence electrons, shifts the Fermi energy away from the gap, which significantly reduces the absolute value of $S(T)$ although the change in the number of valence electrons is rather small.

Summarizing, the DFT results for $S(T)$ resemble the experimental trend rather well. It should be noted that rather small uncertainties in the stoichiometry, which are unavoidable in the preparation of the samples, result in significant variations of the number of valence electrons, which concomitantly leads to substantial variations of the Seebeck coefficients, as demonstrated by Fig. 12.

In Fig. 13 the resistivity $\rho(T)$ is shown for $\text{Ba}_8\text{Cu}_x\text{Si}_{46-x}$ with $x = 4.90 - 5.10$, as derived for frozen- $\text{Ba}_8\text{Cu}_5\text{Si}_{41}$ as the reference. The relaxation time $\tau = 2.32 \times 10^{-14}$ s was chosen to fit the calculated $\rho(T)$ of $\text{Ba}_8\text{Cu}_{5.0}\text{Si}_{41.0}$ to the experimental maximum of $\rho(T)$ of $\text{Ba}_8\text{Cu}_{4.9}\text{Si}_{41.1}$. Inspecting Fig. 13 one realizes that the calculations yield a trend similar to the experimental data, because the characteristic peak shifts toward higher temperatures with decreasing x . The small difference in x between theory and experiment, when requiring good agreement, is attributed to the experimental uncertainties of sample preparation. The maximum in the electrical resistivity is closely related to the position of the Fermi energy. In recent work on $\text{Ba}_8\text{Ag}_x\text{Ge}_{46-x}$, it was found²⁸ that the peak is due to a

particular position of the Fermi level in combination with the temperature dependence of the energy derivative of the Fermi function, $\frac{df(E)}{dE}$. More specifically, if the Fermi energy is above but very close to the gap, the states below the gap will contribute to the electronic transport only for sufficiently large temperatures when $\frac{df(E)}{dE}$ is sufficiently broad. As the Fermi energy moves closer or away from the gap, concomitantly lower or higher temperatures are required for thermally exciting states below the gap. From the discussion above, one derives that the Fermi energies for all the compounds are above the gap and are approaching it as x increases from 4.9 to 5.1.

From the discussion above we conclude, that the thermoelectric properties and the conductivity of $\text{Ba}_8\text{Cu}_x\text{Si}_{46-x}$ alloys can be reasonably described and understood by means of a DFT approach.

IV. CONCLUSION

In summary, thermoelectric properties of the ternary clathrate $\text{Ba}_8\text{Cu}_x\text{Si}_{46-x}$ with the nominal Cu contents $x = 3.6, 3.8, 4.2, 4.4, 4.6, 5, 6, 7$ have been investigated. All thermoelectric quantities vary systematically with the actual Cu content in the clathrate phase. The highest figure of merit $ZT = 0.23$ is achieved for the sample with the nominal composition $x = 6$ at about 450°C . Almost the same ZT is retained over a relatively broad temperature range from 350 to 550°C . For the optimal Cu content, samples were fabricated also by melt spinning. One of these samples reaches an even larger ZT value of 0.28 at 600°C . Extensive density functional theory calculations have been performed. For deriving enthalpies of formation the respective total energies for $\text{Ba}_8\text{Si}_{46}$, $\text{Ba}_8\text{Cu}_x\text{Si}_{46-x}$ and $\text{Ba}_8\text{Au}_x\text{Si}_{46-x}$ were computed. Thermoelectric properties were treated within Boltzmann's theory and the properties in terms of Seebeck coefficients and resistivities were calculated by exploiting the electronic structure of $\text{Ba}_8\text{Cu}_6\text{Si}_{40}$ and $\text{Ba}_8\text{Cu}_5\text{Si}_{41}$. Overall, the agreement between the density functional data and experiment is reasonable, but some discrepancies remain to be solved.

ACKNOWLEDGMENTS

The authors would like to thank M. Wass for assistance in SEM/EDX measurements, A. Grytsiv and M. Falmbigl for help with hot pressing, and A. Prokofiev for fruitful discussions. This work was supported by the FFG project THECLA (815648), and partially by the FWF projects P19458-N16 and TRP 176-N22. M.X.C. gratefully acknowledges the support by the FWF within the Science College W4 "Computational Materials Science".

- * Email address: paschen@ifp.tuwien.ac.at
- ¹ G. A. Slack, *New Materials and Performance Limits for Thermoelectric Cooling*, edited by D. Rowe (CRC Press: Boca Raton, 1995) p. 262.
 - ² P. Rogl, *Handbook of Thermoelectrics, Macro to Nano*, edited by D. Rowe (CRC Press: Boca Raton, 2006) pp. 32–1.
 - ³ S. M. Kauzlarich, S. R. Brown, and G. J. Snyder, *Dalton Trans.* **2007**, 2099 (2007).
 - ⁴ E. S. Toberer, A. F. May, and G. J. Snyder, *Chem. Mater.* **22**, 624 (2010).
 - ⁵ E. Zintl, *Angew. Chem.* **52**, 1 (1939).
 - ⁶ S. M. Kauzlarich, *Chemistry, Structure, and Bonding of Zintl Phases and Ions* (Wiley-VCH: New York, 1996).
 - ⁷ S. C. Sevov, *Intermetallic Compounds, Principles and Practice: Progress*, edited by J. Wiley and Sons (Chichester, England, 2002) p. 113.
 - ⁸ N. Melnychenko-Koblyuk, A. Grytsiv, P. Rogl, E. Bauer, R. Lackner, E. Royanian, M. Rotter, and G. Eister, *J. Phys. Soc. Jpn.* **77**, 54 (2008).
 - ⁹ N. Nasir, A. Grytsiv, N. Melnychenko-Koblyuk, P. Rogl, E. Bauer, R. Lackner, E. Royanian, G. Giester, and A. Saccone, *J. Phys.: Condens. Matter* **21**, 385404 (2009).
 - ¹⁰ C. L. Condon, R. Porter, T. Guo, and S. M. Kauzlarich, *Inorg. Chem.* **44**, 9185 (2005).
 - ¹¹ C. L. Condon, J. Martin, G. S. Nolas, P. M. B. Pocoli, A. J. Schultz, and S. M. Kauzlarich, *Inorg. Chem.* **45**, 9381 (2006).
 - ¹² C. L. Condon, S. M. Kauzlarich, T. Ikeda, G. Snyder, F. Haarmann, and P. Jeglič, *Inorg. Chem.* **47**, 8024 (2008).
 - ¹³ N. Jaussaud, P. Gravereau, S. Pechev, B. Chevalier, M. Menetrier, P. Dordor, R. Decourt, G. Goglio, C. Cros, and M. Pouchard, *C. R. Chimie* **8**, 39 (2005).
 - ¹⁴ N. Mugita, Y. Nakakohara, T. Motooka, R. Teranishi, and S. Munetoh, *IOP Conference Series: Materials Science and Engineering* **18**, 142007 (2011).
 - ¹⁵ N. Tsujii, J. H. Roudeshush, A. Zevalkink, C. A. Cox-Uvarov, G. J. Snyder, and S. M. Kauzlarich, *J. Solid State Chem.* **184**, 1293 (2011).
 - ¹⁶ H. Kawaji, H. Horie, S. Yamanaka, and M. Ishikawa, *Phys. Rev. Lett.* **74**, 1427 (1995).
 - ¹⁷ R. F. W. Herrmann, K. Tanigaki, S. Kuroshima, and H. Suematsu, *Chem. Phys. Lett.* **283**, 29 (1998).
 - ¹⁸ S. Yamanaka, E. Enishi, H. Fukuoka, and M. Yasukawa, *Inorg. Chem.* **39**, 56 (2000).
 - ¹⁹ M. J. Teraoka, Y. Moritomo, and S. Yamanaka, *Nat. Mater.* **2**, 653 (2004).
 - ²⁰ H. Fukuoka, J. Kiyoto, and S. Yamanaka, *J. Phys. Chem. Solids* **65**, 333 (2004).
 - ²¹ L. Yang, Y. Wang, T. Liu, T. D. Hu, B. X. Li, K. Stahl, S. Y. Chen, M. Y. Li, P. Shen, G. L. Lu, Y. W. Wang, and J. Z. Jiang, *J. Solid State Chem.* **178**, 1773 (2005).
 - ²² N. Kamakura, T. Nakano, Y. Ikemoto, M. Usuda, H. Fukuoka, S. Yamanaka, S. Shin, and K. Kobayashi, *Phys. Rev. B* **72**, 014511 (2005).
 - ²³ J. S. Tse, T. Iitaka, T. Kume, and H. Shimizu, *Phys. Rev. B* **72**, 155441 (2005).
 - ²⁴ Y. Li, Y. Liu, N. Chen, G. Cao, Z. Feng, and J. R. Jr, *Phys. Lett. A* **345**, 398 (2005).
 - ²⁵ K. Akai, K. Koga, K. Oshiro, and M. Matsuura, *Trans. Mater. Res. Soc. Jpn.* **29**, 3647 (2004).
 - ²⁶ K. Akai, G. Zhao, K. Koga, K. Oshiro, and M. Matsuura, In: *Proceedings of 24th International Conference on Thermoelectrics*, Beijing, China, IEEE, Piscataway, NJ, USA, 230 (2005).
 - ²⁷ X. Yan, G. Giester, E. Bauer, P. Rogl, and S. Paschen, *J. Electron. Mater.* **39**, 1634 (2010).
 - ²⁸ I. Zeiringer, M. Chen, I. Bednar, E. Royanian, E. Bauer, R. Podloucky, A. Grytsiv, P. Rogl, and H. Effenberger, *Acta Mater.* **59**, 2368 (2011).
 - ²⁹ Utility models in Austria (10749) and Germany (20 2008 006 9467), patents filed in Japan (135 994/2008) and USA (2/231. 183).
 - ³⁰ S. Paschena, C. Gspanb, W. Groggerb, M. Dienstlederb, S. Laumann, P. Pongratza, H. Sassika, J. Wernischa, and A. Prokofieva, *J. Cryst. Growth* **310**, 1853 (2008).
 - ³¹ J. Rodriguez-Carvajal, *FULLPROF: A Program for Rietveld Refinement and Pattern Matching Analysis* (at the Satellite Meeting on Powder Diffraction of the XV IUCr Congress, 1990) p. 127.
 - ³² G. Kresse and J. Furthmüller, *Phys. Rev. B* **54**, 11169 (1996).
 - ³³ G. Kresse and J. Furthmüller, *Comput. Mater. Sci.* **6**, 15 (1996).
 - ³⁴ P. E. Blöchl, *Phys. Rev. B* **50**, 17953 (1994).
 - ³⁵ G. Kresse and D. Joubert, *Phys. Rev. B* **59**, 1758 (1999).
 - ³⁶ H. J. Monkhorst and J. D. Pack, *Phys. Rev. B* **13**, 5188 (1976).
 - ³⁷ G. K. Madsen and D. J. Singh, *Comput. Phys. Commun.* **175**, 67 (2006).
 - ³⁸ N. Melnychenko-Koblyuk, A. Grytsiv, P. Rogl, H. Schmid, and G. Eister, *J. Solid. State Chem.* **182(7)**, 1754 (2009).
 - ³⁹ L. T. K. Nguyen, U. Aydemir, M. Baitinger, E. Bauer, H. Borrmann, U. Burkhardt, J. Custers, A. Haghighirad, R. Hüfler, K. D. Luther, F. Ritter, W. Assmus, Y. Grin, and S. Paschen, *Dalton Trans.* **39**, 1071 (2010).
 - ⁴⁰ N. Melnychenko-Koblyuk, A. Grytsiv, P. Rogl, H. Schmid, and G. Giester, *J. Solid State Chem.* **182**, 1754 (2007).
 - ⁴¹ N. Melnychenko-Koblyuk, A. Grytsiv, S. Berger, H. Kaldarar, H. Michor, F. Röhrbacher, E. Royanian, E. Bauer, P. Rogl, H. Schmid, and G. Eister, *J. Phys: Condens. Matter* **19**, 046203 (2007).
 - ⁴² N. Melnychenko-Koblyuk, A. Grytsiv, P. Rogl, M. Rotter, R. Lackner, E. Bauer, L. Fornasari, F. Marabelli, and G. Eister, *Phys. Rev. B* **76**, 195124 (2007).
 - ⁴³ A. Prokofiev, J. Custer, M. Kriegisch, S. Laumann, M. Müller, H. Sassik, R. Svagera, M. Waas, K. Neumaier, A. M. Strydom, and S. Paschen, *Phys. Rev. B* **80**, 235107 (2009).
 - ⁴⁴ M. M. Koza, M. R. Johnson, H. Mutka, M. Rotter, N. Nasir, A. Grytsiv, and P. Rogl, *Phys. Rev. B* **82**, 214301 (2010).
 - ⁴⁵ H. Zhang, H. Borrmann, N. Oeschler, C. Candolfi, W. Schnelle, M. Schmidt, U. Burkhardt, M. Baitinger, J.-T. Zhao, and Y. Grin, *Inorg. Chem.* **50**, 1250 (2011), <http://pubs.acs.org/doi/pdf/10.1021/ic1016559>.
 - ⁴⁶ E. Parthé, L. Gelato, B. Chabot, M. Penzo, K. Cen-zual, and R. Gladyshevskii, *TZPIX Standardized Data and Crystal Chemical Characterization of Inorganic Structure Types* (Springer, 1994).
 - ⁴⁷ X. Yan, A. Grytsiv, G. Giester, E. Bauer, P. Rogl, and S. Paschen, *J. Electron. Mater.* **40**, 589 (2011).

⁴⁸ M. Cutler, J. F. Leavy, and R. L. Fitzpatrick, Phys. Rev. **133**, 1143 (1964).

⁴⁹ F. J. Blatt, Proc. Phys. Soc. **83**, 1065 (1964).

⁵⁰ R. Peierls, Ann. Phys. **395**, 1055 (1929).